Amplitude adaptive optics with a digital micro-mirror device for exoplanet high-contrast imaging

Alexis Carlotti, Salma Baccar, Lucie Leboulleux, Stéphane Curaba, Alain Delboulbé, Laurent Jocou, Thibaut Moulin, Laurence Gluck, Marie-Helene Sztefek

AO4ELT7 - June 2023 - Avignon

Amplitude adaptive optics with a digital micro-mirror device for exoplanet high-contrast imaging

Alexis Carlotti[a], Salma Baccar[a], Lucie Leboulleux[a], Stéphane Curaba[a], Alain Delboulbé[a], Laurent Jocou[a], Thibaut Moulin[a], Laurence Gluck[a], and Marie-Hélène Sztefek[a]

[a]Univ. Grenoble Alpes, CNRS, IPAG, 38000 Grenoble, France

ABSTRACT

Oncoming exoplanet spectro-imagers like the Planetary Camera and Spectrograph (PCS) for the Extremely Large Telescope (ELT) will aim for a new class of exoplanets, including Earth-like planets evolving around M dwarfs i.e., as close as 0.02" with contrasts around 10^{-8}. This goal can be achieved using coronagraphs. Classical coronagraphs are not optimal, however: 1) they usually impose a planetary photon loss, which is particularly problematic when the instrument includes a high spectral-resolution spectrograph, 2) some aberrations such as the missing segments of the ELT are dynamic and not compatible with a static coronagraph design, 3) the coupling of the exoplanet light into a fiber for spectroscopy only requires the electric field to be controlled on a small target-dependent region of the detector. Such instruments would benefit from an adaptive tool to modulate the wavefront in both amplitude and phase. We propose to combine in the pupil plane a deformable mirror (DM) to control the phase and a digital micro-mirror device (DMD) i.e., an array made of millions of micro-mirrors able to switch between two positions, to provide a binary amplitude control. If the DM is already well-known in the field in particular for adaptive optics applications, the DMD has so far not been fully considered. At IPAG, we have assembled a testbed called CIDRE (Coronagraphy for DiRect Imaging of Exoplanets) to develop, test, calibrate, and validate the combination of these two components with a Lyot coronagraph. Since mid-2022, the testbed is operational and has entered its scientific exploitation phase albeit without the Lyot coronagraph yet, to test dynamic amplitude apodization coronagraphs (so-called Shaped Pupils).

Keywords: Exoplanet, direct imaging, high contrast, coronagraphy, adaptive optics

1. INTRODUCTION

The study of exoplanets proposes to better understand their formation mechanisms, their diversity, and assess their habitability. This study relies in practice on the spectral analysis of the light of planets. This information can be obtained for transiting planets, although the short time during which observations can be made requires potentially large number of observations to reach a sufficiently high signal-to-noise ratio.

For further author information, send correspondence to A. Carlotti: alexis.carlotti@univ-grenoble-alpes.fr

High angular observations makes it possible to increase the SNR by resolving the planet, and thus lower the photon noise of the star at its location. Adaptive optics (AO) is used to control the wavefront, and coronagraphy to lower the relative intensity of the diffracted light next to the star. Combined, they enable what is referred to as high-contrast imaging. Multiple instruments have been built around these twin techniques, including, but not limited to, VLT/SPHERE[2], GPI[11], SCExAO[9], and MAGAO-X[12]. While those four instruments instruments are ground-based, high-contrast imaging is also possible from space: JST's NIRCAM[7] and MIRI[20] use coronagraphs, and NGRST's coronagraphic instrument (CGI[15]) will demonstrate advanced wavefront control in space. It is a technological demonstrator for the Habitable World Observatory (HWO), whose main objective will be to study the habitability[19] of rocky planets around nearby stars.

The near-future 25-40m Extremely Large Telescopes (ELTs) will offer an angular resolution up to 4 times finer than the one offered by the largest optical ground-based telescopes. Their instruments will be able to observe planets at smaller physical distances, below the snow line, and formation regions that are located further away from our solar system.

These unprecedented telescope diameters are made possible thanks to the segmentation of the primary mirror. The European ELT will use 798 1.5m-large segments. Each segment will be actuated in piston, tip, and tip for cophasing. It is expected that a few actuators will fail each night, however, in which case these faulty segments will be manually tilted so that they do not send light in an uncontrollable way towards the instruments.

Missing segments will induce a fringe pattern in the point-spread function (PSF) of the telescope, and it will change from one night to the other in an unpredictable way. With a a relative intensity of $\sim 10^{-5}$, it should not be a critical issue for instruments looking at young giant planets in proper emission, which display flux ratio down to $\sim 10^{-6}$ relative to their star, but it could become one when trying to observe old rocky planets in reflected light, with $\sim 10^{-8}$ flux ratio relative to their star.

Adapting the instrument to this type of discontinuous amplitude errors, and to the reflectivity errors of the primary would require a dedicated, controllable device. Such a device would also be useful to apodize the pupil, i.e., to locally lower the relative intensity of the diffracted light of the star. It could be used together with focal plane masks, or other pupil plane masks, to create either large or small dark zones next to the star while masking its core. In the latter case, it could be especially useful for instruments such as KPIC and HiRISE that use a monomode fiber connected to a high-resolution spectrometer to characterize the light of planets with a known location.

A low-order amplitude control technique has already been proposed and tested in the laboratory. It is thought as an extension to classical wavefront control, i.e., a way to correct for small amplitude errors in a high-contrast imaging system [18], or as a beam shaping technique helping coronagraphs work in spite of aperture discontinuities [17, 14]. It can be seen as an active phase-induced amplitude apodization (PIAA) technique [8]: instead of using pairs of PIAA mirrors (or lenses), it uses a pair of deformable mirrors (DM) in non-conjugated planes. The first DM induces a phase modulation that induces a mix of phase and amplitude modulations in the plane of the second DM thanks to the free-space propagation of the electric field between the two DMs, and the second DM corrects for the residual phase modulation. The dynamics and the spatial frequency of these amplitude modulations are limited by the numbers of actuators, and by the physics involved in the modulation.

An alternative way to control the amplitude is to use a micro-mirror array (MMA), i.e., an array of hundreds to thousands of micron-size mirrors that can each move independently from the others. In particular, mirrors capable of tilting can redirect light towards a preferential direction, or another. A specific type of MMA is the digital micro-mirror devices (DMD) produced by Texas Instrument (TI). They use bi-stable micro-mirrors to selectively transmit light towards two possible directions, thus offering a binary control of the amplitude of a beam. This technology was first investigated for astronomy with the objective of selecting sources in a multi-object spectrograph [21]. Its application for high-contrast imaging is more recent [4, 10]. Its aim is to provide adaptive apodization capable of satisfying the constraints set by the telescope (complex shape with changing discontinuities), and by the observation objectives. First tests had identified the need to use a DMD together with an AO system because of strong low-order aberrations induced by the DMD, and the dispersive nature of DMDs, which restricts their use to monochromatic light.

The aim of the present study is to test in the laboratory the amplitude control capability of a DMD, and its interest for high-contrast imaging, to explore its limitation, and to look for possible alternatives to the current technology. A dedicated testbed has been installed to test a DMD, and its design and components are presented in sec.2. The operation of the adaptive optics system, both to correct for the low-order aberrations of the DMD, and for other wavefront errors, including non-common path aberrations, is detailed in sec.3. Sec.4 presents the results of the use of the micro-mirror device as an adaptive apodizer, and studies the effect of stray light induced by the device. Sec.5 concludes on these tests, and discusses recent technological developments including an achromatic amplitude control and piston MMA which should benefit high-contrast imaging and adaptive optics.

2. TESTBED DESIGN

2.1 Layout

The CIDRE testbed aims at applying, testing, and calibrating the use of a DMD as an adaptive amplitude controller and pupil apodizer. The optical design of the testbed is shown in Fig.1. It includes:

- a 635 nm fibered, stabilized LASER source, which defines the first focal plane, and whose light is then collimated with a doublet,
- a low-order DM, and a DMD, located in conjugated pupil planes, with pupil diameters of 13.5 and 10.8mm, respectively,
- focal plane masks (FPM), located at a focus with an F/D=25 ratio,
- a Shack-Hartmann (SH) wavefront sensor located in a pupil plane conjugated to the DM and DMD, with a 10.8mm pupil diameter, and which is fed with a pick-off mirror that can be deployed or removed remotely,
- Lyot stops, located in the same pupil plane, and which mask the beam when it is not fed to the SH-WFS,
- a camera, located in a focal plane with an F/D=25 ratio.

With this choice of components, two coronagraphs can be used: Shaped Pupils, and Apodized Pupil Lyot Coronagraphs (APLCs). For now, the FPM and the Lyot stops are not set up, however, and the testbed is only used in the Shaped Pupil mode.

The deformable mirror, in addition to correcting for quasi-static aberrations, will also be used for adaptive phase control, to compare the relative performance of amplitude and phase apodizations, and to test complex apodization where the DMD and the DM are combined.

Note that pupil images can be obtained with the camera by moving it in the pupil plane where the Lyot stop should be located. Examples of pupil images are given in the next section.

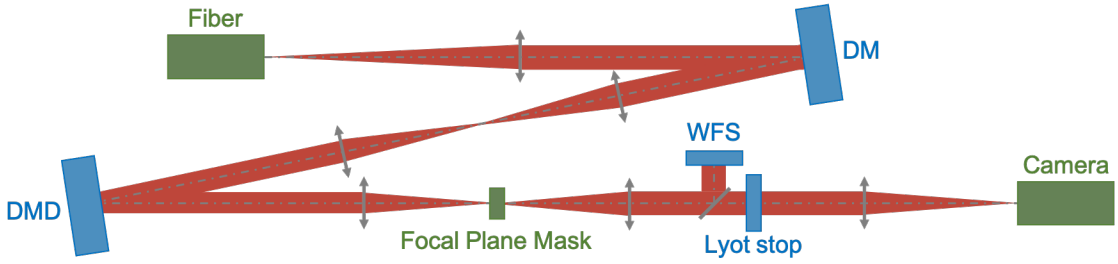

Figure 1: General design of the CIDRE testbed. The red beam is reflected or transmitted by pupil plane components (in blue), and focal plane components (in green).

2.2 Components specifications

The DMD is a V-9501 model from Vialux, and which is based on the Digital Light Processing (DLP) technology from TI. It has a surface of 20.7×11.7 mm^2 [1], and it is composed of 1920×1080, $10.8\mu m$-large, square aluminum mirrors. Each mirror can flip between two states, $\pm 12°$ with respect to the normal of the array, and along one of their diagonal. The flat (0°) direction cannot be controlled, so the overall surface forms a periodic pattern similar to the one of a blazed grating which strongly disperses a polychromatic beam. This effect has limited our previous results [10]. In addition, the DMD surface generates a large low-order aberration (a $0.25\mu m$ RMS was previously reported [4]) which requires a DM to be corrected.

The pupil size in the plane of the DMD is 10.8mm, which translates into a maximum of almost 1000 micro-mirrors along the pupil diameter. For the ELT pupil, for instance, this means that each of the 1.5m segment of the primary mirror projects onto a maximum of almost 39 micro-mirrors, and the 0.5m spiders of the ELT project onto almost 13 micro-mirrors. Fig.2 illustrates the capability of the DMD to control the pupil plane amplitude. A negative image of the ELT pupil is displayed onto the DMD, which makes it possible to both take a look at the beam reflected off the DM optical surface (and then on the DMD), and at the exquisite spatial resolution with which the ELT pupil is sampled with the DMD. Indeed, even though the ELT pupil is projected onto ~ 850 micro-mirrors across its diameter, each of the ELT segment is projected onto ~ 33 micro-mirrors. Seven missing segments are taken into account in this pupil, and one can appreciate the level of details with which they are reproduced. The elliptic shape of the beam is due to the non-zero incident angle of the light onto the DM.

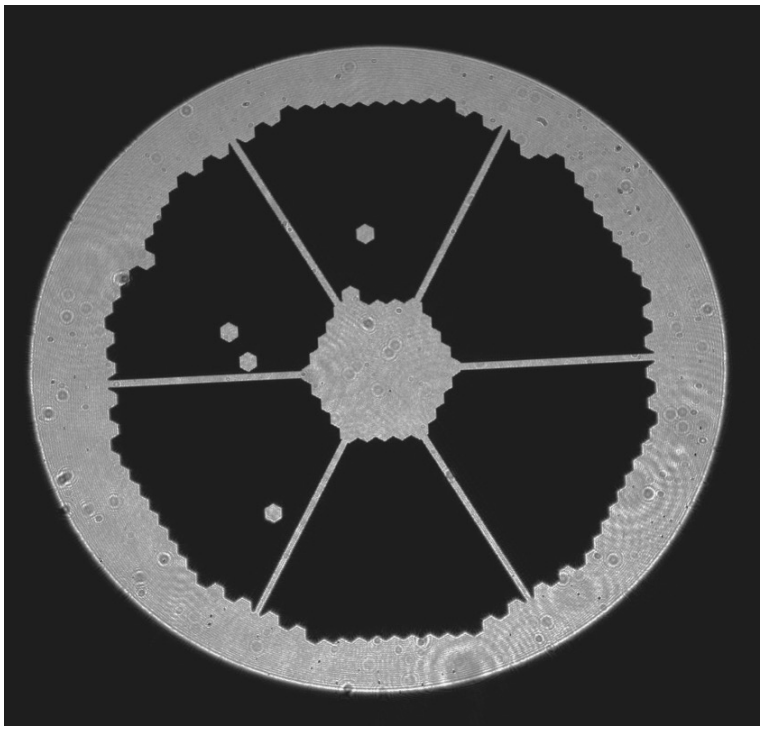

Figure 2: Image of the beam in the pupil plane. The DMD is controlled in this case to send away from the camera the light within the ELT pupil. This highlights the beam that comes from the DM and which is reflected onto the DMD and towards the camera. The elliptic shape of the beam is related to the incidence angle of the light onto the DM. The negative ELT pupil is displayed on the DMD with a smaller size than the beam, resulting with a number of micro-mirrors across the pupil diameter close to 850. Each ELT segment is thus projected onto 33 micro-mirrors.

The blazed grating-like surface of the DMD prevents the use of a broadband source, even with a narrow bandwidth. Tests with a 635nm fiber-coupled laser diode were not satisfying: it produced a forest of lines that

resulted, in the final focal plane, into multiple PSFs with similar intensities, and separated by a few λ/D. We chose to work with an Helium-Neon laser from Thorlabs (HRS015B model). It is centered on a 632.992nm wavelength, and its frequency can be stabilized to ensure that only a $1-2$MHz change, i.e., a $1.3-2.7\,10^{-6}$nm drift can be observed over 1h.

The correction of the low-order aberrations induced by the surface errors of the DMD (and by other optical surfaces, and because of optical misalignments) is performed by an ALPAO 97-15 DM. The controllable surface is a disk with a 13.5mm diameter, with 11 actuators across separated by a 1.5mm pitch. The total number of actuators is 97. Due to this actuator density, the wavefront can be corrected up to $5-5.5\lambda/D$ (although in practice the continuous membrane of the DM makes it possible to correct the impact of low-order aberrations further away from the star).

Wavefront errors are measured thanks to a Shack-Hartmann sensor with a 73x73 lenslets array, corresponding to a maximum 11.26mm beam diameter. In practice the maximum beam diameter is 10.8mm, which corresponds to about 70 lenslets. That means that aberrations up to $35\lambda/D$ can be measured. This is significantly above the spatial cut-off frequency of the DM, and while one wants to keep the frequency domain of the WFS a bit larger than the one of the DM, there would likely be an interest in having a lower number of lenslets if the flux received by the WFS was too low. This is not the case here, however, and this high spatial resolution capability is not an issue. Note that a phase offset derived from the calibration of the WFS (performed using a collimator) is automatically subtracted from the WFS data to remove a systematic bias.

The camera is an ASI2600 monochrome device from ZWO. It has over 4000 by 6000 $3.76\mu m$ large pixels. Given the source wavelength, and the maximum pupil diameter, the pixel size is about $\lambda/4D$, which twice as enough to satisfy the Nyquist sampling criterion. Note that, because the DMD can lower the effective pupil diameter, the sampling can change, and we keep it larger than half of the maximum diameter to always provide a high-enough sampling of the PSF. Only a fraction of the image is read when imaging the PSF - the region of interest is only $\sim 100\lambda/D$ wide, which corresponds to ~ 400 pixels - but the large size of the sensor is needed to image the pupil, and the pixel size makes it possible to image each micro-mirror of the DMD with more than 2 camera pixels.

3. WAVEFRONT CONTROL

As presented in sec.2, the AO system uses a SH WFS, and a low-order DM to sense and compensate wavefront errors. Using an interaction matrix, the WFS data is used to derive the commands that are applied on the DM through its control electronics. The non-common path aberrations between the WFS and the science camera are estimated through a focal-plane wavefront sensing method which we detail thereafter.

3.1 Adaptive optics loop

We establish an interaction matrix (IM) to calibrate the interaction between the DM and the SH WFS, i.e., how an actuator's command is seen by the WFS. During this process, a piston command is sent to the DM, i.e., by pushing each actuator with the same amplitude. All the other commands are added to this piston command. The value of the piston command is commonly chosen to be 1/4 or 1/2 of the maximum stroke of the DM. The rest of the process is done iteratively:

1. a positive command is given to the ith actuator (1/4 of the maximum stroke if the piston command is set to 1/2, or 1/8 if the piston command is set to 1/4), and the wavefront $SH_{i,p}$ is measured by the SH WFS,
2. a command with the same amplitude but with an opposite sign (negative) is sent to the same ith actuator, and the wavefront $SH_{i,n}$ is measured by the SH WFS,
3. the wavefront measurement SH_i for the ith actuator is derived though the following equation: $SH_i = 0.5 \times (SH_{i,p} - SH_{i,n})$.

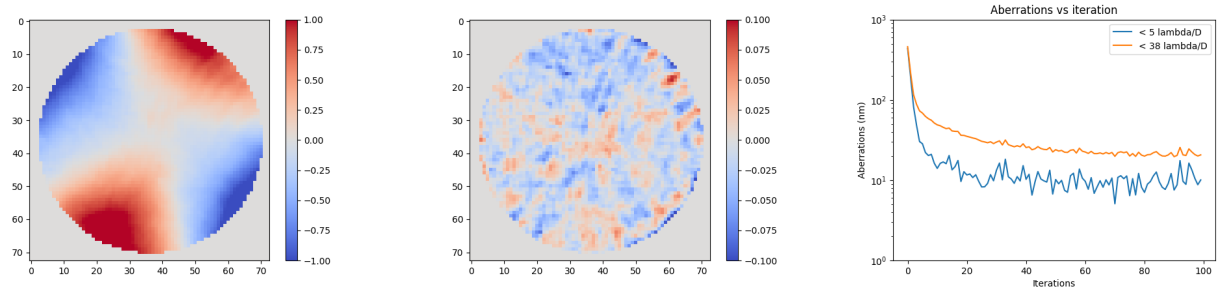

(a) The initial wavefront (b) The final wavefront (c) Aberrations measurements

Figure 3: Closed-loop correction. From left to right: initial wavefront as measured by the SH WFS (in microns), corrected wavefront after 100 iterations, and evolution of the amplitude of the aberrations over a hundred iterations, for $0-5$ cyc/pup (blue line) and $0-38$ cyc/pup aberrations (orange line). The correction process lowers the wavefront aberration from $\sim$ 500nm RMS down to $\sim$ 20nm RMS.

The 97 *SH* measurements are turned into vectors, which then form the IM. Subsequently, the control matrix (CM) is computed by taking the pseudo-inverse of the IM. To correct the wavefront in closed loop, the command vector that is sent to the DM is computed by taking the product of the CM and a new wavefront error vector measured by the SH WFS.

The wavefront errors measured by the WFS before the loop is closed (fig. 3a), and at the end of the loop (fig. 3b) are showed side by side. A strong astigmatism is present before the correction is performed. Nevertheless, through the derivation and the application of successive corrections by the AO system, the wavefront is significantly corrected: the wavefront aberration is lowered from $\sim$ 500nm RMS down to $\sim$ 20nm RMS. This is illustrated in fig. 3c, which displays the residual root mean square (RMS) error iteration by iteration, for two spatial frequency regimes to highlight the reduction of low-order aberrations (below 5 cycles per pupil), and of the total aberrations that can be measured by the SH WFS. In particular, the low-order residual aberrations at the end of the correction are $\sim$ 10nm RMS.

The loop is closed while using a 0.8 loop gain. While most of the low-order aberrations are corrected within less than 5 iterations, it takes about 20 iterations for the low-order residuals to reach a plateau, and it takes about 50 iterations for the total residual aberrations to reach a plateau.

3.2 NCPA correction

The non common path aberrations (NCPAs) refers to the residual aberrations that result from the difference between the wavefront errors that are measured by the WFS, and those that effectively induce the intensity aberrations, i.e., the speckles in the final image plane, as measured by the science camera. They result from the fact that (a) the light follows different paths in the optical system to reach either the SH WFS or the science camera, and (b) the WFS measurement may suffer from a residual bias.

NCPA must be kept low enough to measure a low enough flux ratio in the dark hole created by the apodization pattern around the star, relative to its peak intensity.

Estimating NCPA is done through a common-path measurement: the differential aberrations must be measured directly on the science camera. In practice we use the DM to sequentially introduce additional wavefront errors: Zernike modes of various amplitudes and shapes. For each aberration pattern and amplitude, we estimate the PSF quality by taking an image with the camera, and measure the PSF peak intensity. Our objective, for each Zernike mode, is to then identify the amplitude value that maximizes the peak intensity of the PSF.

We developed a code to successively introduce 30 different Zernike modes on the DM. Each Zernike mode represents a specific type of wavefront distortion commonly encountered in optical systems, and together they form an orthogonal basis that can ideally be used to decompose any 2D shape. For each Zernike mode, we test amplitude values ranging from -0.2 to 0.2 µm RMS, as illustrated in fig.4. By modulating the DM with

the prescribed amplitudes, the wavefront of the incident light is intentionally manipulated to induce controlled aberrations.

Following the application of each amplitude, the camera captures the resulting PSF of the optical system, characterizing the spatial distribution of the light after it goes through the system. We analyze the PSF image to extract its peak intensity. This information allows us to quantify the quality of the optical system's performance for each combination of Zernike mode and amplitude. The code effectively identifies the appropriate combination of Zernike modes that should be added on the DM surface to enable a precise compensation of the NCPA.

This assumes that the Zernike modes that are reproduced on the DM surface are indeed orthogonal, which may be the case for a clear circular aperture, but is likely not for an apodized one. In addition, the command derived at the end of the closed loop correction of the wavefront is constantly applied onto the DM, and we expect that the effective deformation of the mirror membrane changes over time. While the code that is run to estimate the NCPA is quite fast, it is likely that, to some extent, the NCPA that should be measured change during the measurement. This should result in a limited estimation and correction accuracy.

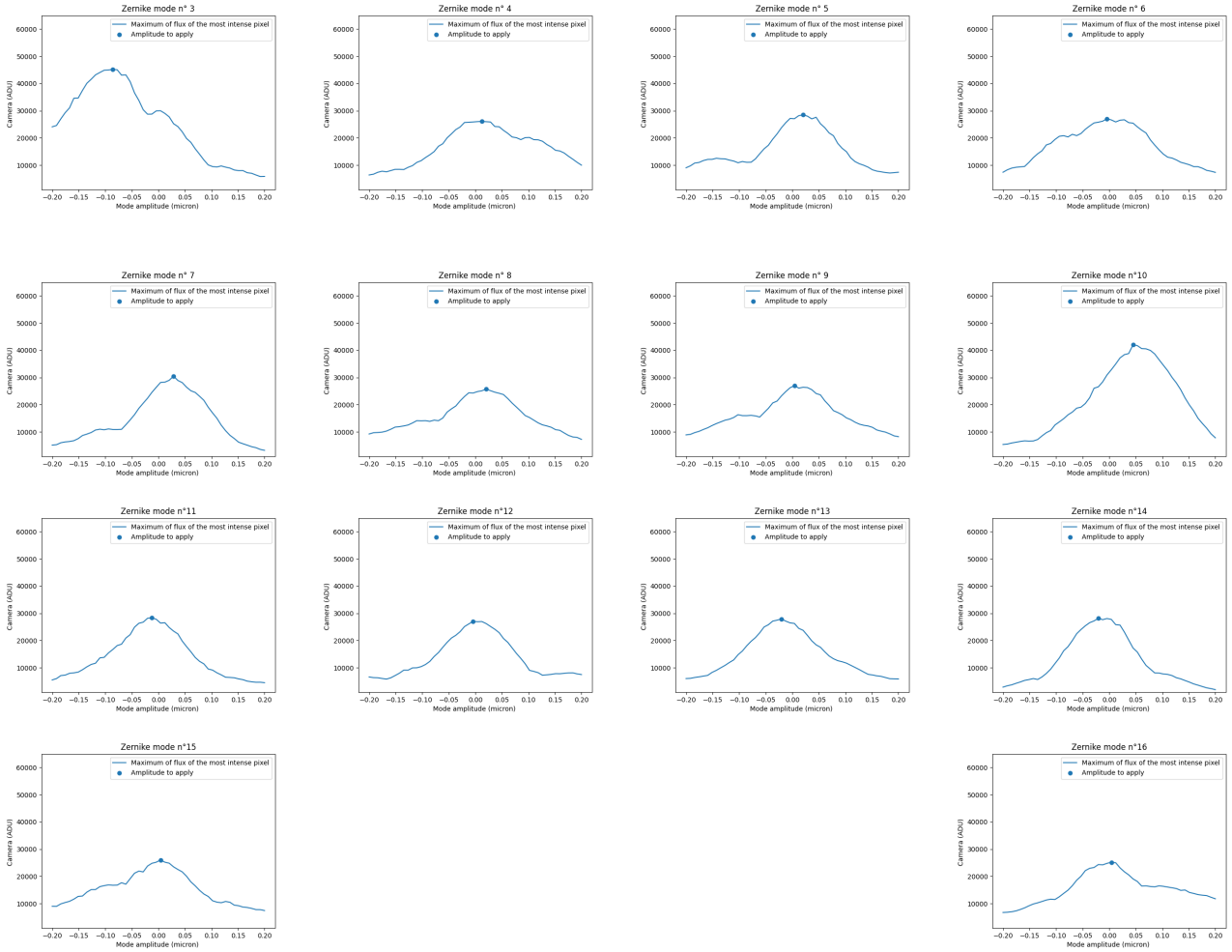

Figure 4: Zernike modes amplitudes vs camera capture of brightest pixel.

Nonetheless, these amplitudes are extracted and assembled into a command vector to correct for the NCPA. It is combined with the command vector obtained at the end of the closed-loop process. When juxtaposed with Fig.5, the PSF exhibits a notable enhancement, boasting a 38% increase in Strehl ratio. In practice, out of the 30

modes that we initially planned to test, we only use the first 12 modes as the impact of the higher-order modes on the PSF peak intensity could not be measured accurately.

(a) (b)

Figure 5: ELT's pupil PSF. (a): PSF with AO correction. (b): PSF with AO correction and NCPAs correction

4. ADAPTIVE APODIZATION

We have checked the capability of the DMD to apodize the beam by displaying pre-computed shaped pupils apodization patterns with its mirrors, and capturing images with the science camera. The computation of these patterns is performed by solving a constrained quadratic optimization problem [3]. We made the choice to design shaped pupils that typically create a dark hole in which the diffracted intensity is 10^{-6} relative to the peak intensity of the apodized PSF. The range of the camera, however, is not high enough to measure with a single image the relative flux ratio between the peak and the dark hole, and images with different exposure times must be taken, and combined together to derive a composite image with a sufficiently large dynamic range.

4.1 Image recombination

The high dynamic image reconstruction process harnesses a series of captured images acquired with various exposure times. Indeed, for a given exposure time only part of the image contains a signal induced by a flux that is both large enough with respect to the readout noise and dark current, and low enough with respect to the saturation level of the detector. The recombination of the entire set of images helps in recovering and normalizing the signal in the entire field-of-view (each exposure time can be associated with a specific region of the field of view, which is partially complementary from the others).

First, a sequence of 100 PSF images is taken with the camera for each designated exposure duration, as presented in fig. 6. Corresponding sequences of dark frames are acquired. Each set of images is averaged, and the dark frames are subtracted from the PSF images to remove the camera's inherent dark current and the background signal from the bench, and the residual noise is lowered through the averaging process.

Subsequently, pixel by pixel, the values, if they fall within the linearity range of the camera, are normalized by the associated exposure time and averaged. The resulting image then displays a high enough dynamics, suitable for the study of the high-contrast PSF created with the DM and the DMD.

4.2 Results

As stated before, we used pupil apodization to overcome the challenge of imaging a faint off-axis source such as a planet located next to a much brighter star by lowering locally the photon noise of the star induced by its diffracted light. The apodization patterns that we use are shaped pupils designed for the High-Contrast Module of ELT/HARMONI[5]. HARMONI is the first-light, visible and near-infrared integral field spectrograph of the ELT. By taking advantage of the 40m diameter of the telescope and a single-conjugated adaptive optics system, it will provide images with an unprecedented spatial resolution, and will benefit from a much higher collecting power than the current $8-10$m-class telescopes. The characterization of exoplanets' atmospheres is one of the many science cases that HARMONI will tackle, with the aim of better understanding planet formation, and obtaining a global view of exoplanets' diversity.

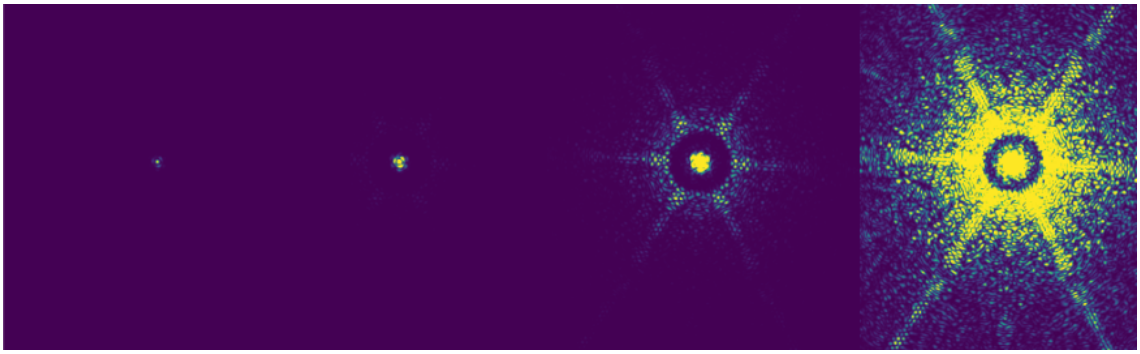

Figure 6: Averaged images of the apodized PSFs obtained with the HSP1 shaped ELT pupil designed for the High-Contrast Module of ELT/HARMONI. The four images correspond to four increasing exposure times, each providing data with the right SNR for a given region of the image plane.

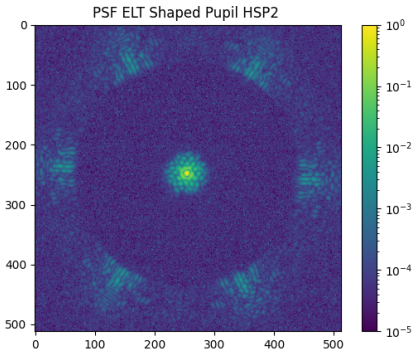

Figure 7: Composite image of an apodized PSF created with the HSP2 shaped ELT pupil designed for the High-Contrast Module of ELT/HARMONI.

The CIDRE testbed makes it possible to replicate the two binary apodization patterns of HARMONI's shaped pupils, to factor in the absence of some of the primary mirror segments, and to test the ability of the DMD to update its display to correct for these missing segments. In the latter case, the apodization pattern has been modified to fit the M1 amplitude aberrations. This is done through a similar numerical optimization process as the one used to design the shaped pupils that assume a nominal M1, and the properties of the high-contrast region are set to be very similar, if not the same.

Note that pupils are displayed on the DMD with about 850 micro-mirrors across the pupil diameter, while ELT/HARMONI's shaped pupils are designed with 1024 pixels across. Their pattern is interpolated, and the resulting non-binary transmission is forced to be binary using an error diffusion algorithm similar to the one that was used to convert the grey prolate apodizers of VLT/SPHERE into binary apodizers, i.e., microdot apodizers[13]. The interpolation process also takes into account the pupil anamorphosis due to the non-zero incidence angle of the light reflecting off the DMD surface, as well as the small clocking of the DMD array with respect to the camera pixel array.

Fig.8 and 9 display the pupil apodization patterns prior to their interpolation. They are not pupil images obtained with the camera, and serve to highlight the differences between the designs of the shaped pupils in the absence, and the presence of missing segments.

The high-contrast region where diffracted light is reduced by the shaped pupils stretches from an Inner Working Angle (IWA) of $5\lambda/D$ to an Outer Working Angle (OWA) of about $12\lambda/D$ for Shaped Pupil 1 (HSP1). For HSP2, the IWA and OWA are $7\lambda/D$, and $38\lambda/D$, respectively.

The IWA denotes the narrowest angular separation from the star for which at least half of the PSF of the planet falls in the high-contrast region created by the shaped pupil. Conversely, the OWA establishes the widest angular separation beyond which the shaped pupil's ability to hinder starlight diminishes.

The apodization patterns are such that they should lower the maximum intensity of the diffracted light in the high-contrast region to 10^{-6} relative to the peak intensity of the PSF, in the absence of wavefront or amplitude aberrations. The absence of a few segments creates interference fringes in the image plane, and Fourier optics simulations indicate that M1 aberrations should increase the relative intensity to $\sim 10^{-5}$.

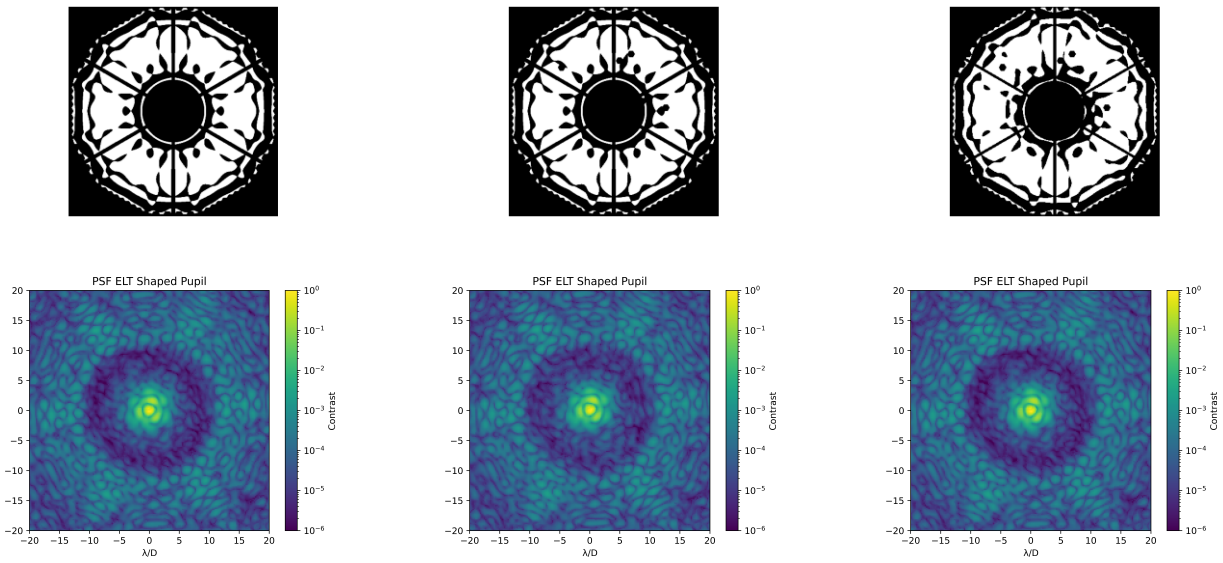

(a) Initial apodizer (b) Same apodizer, with M1 aberrations (c) Modified apodizer design

Figure 8: Apodization patterns (top), and apodized PSF (bottom). From left to right: (a) case of HSP1 without M1 amplitude aberrations. (b), same shaped pupil but with missing segments. (c): modified HSP1 design taking into account the same missing segments. Low order aberrations limit the contrast in the 5-12λ/D region to a few 10^{-5} relative to the peak intensity, and there are only subtle differences between the three PSF.

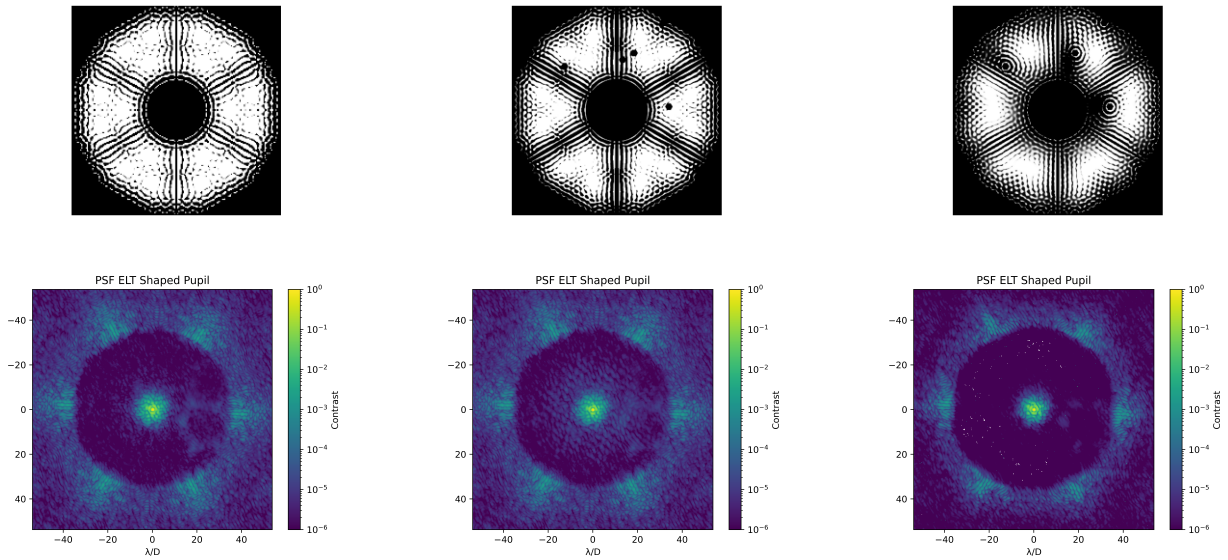

(a) Initial apodizer (b) Same apodizer, with M1 aberrations (c) Modified apodizer design

Figure 9: Apodization patterns (top), and apodized PSF (bottom). From left to right: (a) case of HSP2 without M1 amplitude aberrations. (b), same shaped pupil but with missing segments. (c): modified HSP2 design taking into account the same missing segments. The fringes induced by the missing segments clearly appear in fig.9b, and are efficiently corrected by the modified HSP2 design. A defocused ghost can be seen on the right side of the PSF, at about $22\lambda/D$ from the its center.

Residual low order aberrations make it difficult to properly assess the differences between the PSF induced by the HSP1 apodizing patterns showed in fig. 8a, although subtle differences can be observed between the three cases. The average contrast is a few 10^{-5} relative to the peak intensity. It becomes higher when missing segments are added to the apodization pattern, and the modification of the design of the HSP1 shaped pupil - to take into account the missing segments - restores the properties of the original HSP1 PSF.

The average contrast in fig. 9a is around 6×10^{-6} without M1 amplitude aberrations, and excluding the defocused ghost that can be seen on the right side of the PSF, and which displays a 10^{-5} intensity relative to the peak. When segments are missing, more light is observed in the high-contrast zone, as seen in fig. 9b where the average contrast is about 10^{-5}. In the last figure, fig. 9c, the missing segments are taken into account in the design of the shaped pupil to restore the quality of the initial contrast. The measured average is around 5×10^{-6} which is almost identical to the one measured in the original HSP1 PSF.

The residual wavefront aberrations measured with the SH WFS after a hundred iterations of a closed loop could well explain the relative intensity of the light within the high-contrast region. As detailed in sec.3, there is 15nm RMS of low-order aberrations (¡$5\lambda/D$), and 20nm RMS of aberrations for spatial frequencies up to $36\lambda/D$. Numerical models [5] indicate that such amplitudes can increase the relative intensity of the diffracted in the high-contrast region created by a shaped pupil to a few 10^{-6}, or even 10^{-5} relative to the peak intensity of the apodized PSF, depending on the separation to the center of the PSF. The power spectral density (PSD) profile of the wavefront aberrations likely changes the correspondence between contrast and aberrations amplitude, and this model assumes an f^{-2} PSD, where f is the spatial frequency of the aberrations.

4.3 DMD-induced stray light and ghost

The design and the operation of a DMD are very different from the one of a classical apodizer, and it can be a source of stray light. It is important to characterize it to understand whether this device is compatible or not with the constraints of high-contrast imaging. In particular, one may want to know how this stray light compares to the relative intensity of the planets that would be looked for, next to the star.

We attempt to experimentally measure the amount of stray light by controlling the DMD to send all of the light away from the science path ("all off" state), and measure how much light still reaches the camera. Using the science camera we record a series of exposures with various exposure times, in the same fashion as what was described in the previous section when acquiring high-contrast PSFs. In a second time we do the same while controlling the DMD to send all light along the science path ("all on" state).

A comparison of the two PSFs is given in fig.10. We observe a faint ghost PSF in the "all off" state of the DMD. Its peak intensity is 1.3×10^{-5} relative to the peak intensity of the "all on" PSF, and its spatial distribution is very similar. In addition, its location in the focal plane is the same.

The intensity of the "all off" PSF does not decrease in an identical way to the one of the "all on" PSF, and the former appears to reach a plateau with an intensity, at a $20\lambda/D$ separation, of $\sim 10^{-9}$ relative to the peak of the "all on" PSF, which is $\sim 10^{-4}$ relative to the peak of the "all off" PSF. By comparison, the intensity of the "all on" PSF is $\sim 10^{-5}$ relative to its peak at the same separation. This plateau might be an artefact of the camera, given the very long exposure time that is required.

At a $5\lambda/D$ separation, the relative intensity of the ghost PSF is $\sim 10^{-8}$. It is $\sim 2\,10^{-7}$ at $2\lambda/D$, and $\sim 10^{-6}$ at $1\lambda/D$. While these values are quite low, they may not be negligible when trying to characterize a rocky planet very close to its star. It is all the more important to understand the origin of this PSF to propose potential mitigation strategies.

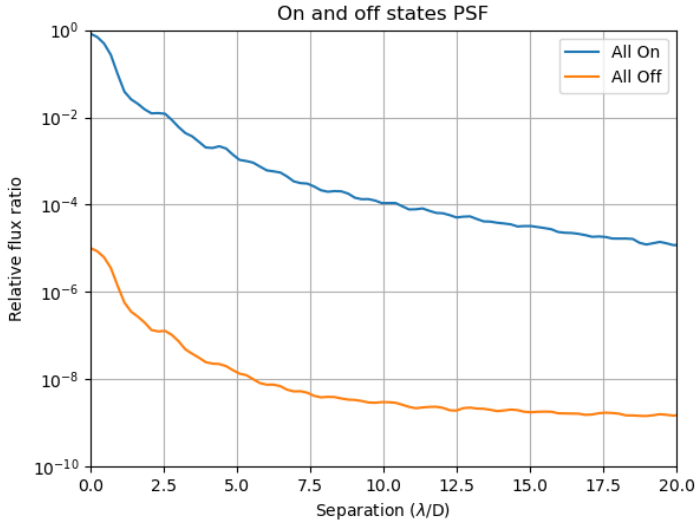

Figure 10: PSF of the beam with the DMD set to an "all on" state (blue line), and "all off" state (red line). No apodization pattern is applied in the "all on" state, for which the effective aperture is limited by the diameter of the DM reflective area.

We do not expect the DMD to be a significant source of stray light, although, given the surface temperature of the device, which is not cooled down, it could be an issue if we were observing in the thermal infrared, or even in the K band. We have not considered this particular point in our study, however.

The origin of the ghost PSF observed on the testbed is more likely related to the control properties of the DMD, as the following analysis appears to confirm.

The DMD may induce a peculiar type of ghost related to the periodic refresh of the array. During a brief amount of time, mirrors that should not send light towards the science path may do so, and this may result in a contrast loss, i.e., a relative intensity of the diffracted light that is higher than it should be. The camera control can by synced with the DMD, and short exposures obtained with the camera can be obtained when the DMD is stable. This is not possible for exposures longer than the refresh period, however. Given the ratio between the

refresh time τ, and the refresh period T, one can model the peak-to-peak ratio between the un-apodized PSF and the apodized PSF as τ/T.

In our case T is set to $1s$, which is the longest time allowed by the current SDK of the DMD. The value of τ is not entirely clear to us. According to the manufacturer, it takes $\sim 56\mu s$ for the pattern to be refreshed over the whole array. That time actually includes the time it takes to load the new pattern (which, in our case, is the same), to globally refresh the mirrors, and for the mirrors to settle to their new state. The actual time τ during which the mirrors move is not known, although the manufacturer also refers to a mirror switching time of $\sim 12.5\mu s$ that characterizes the minimum amount of time between two successive commands given to an individual mirror, and it includes the time for the mirror to move, and the settling time. We assume that the global refresh time cannot be smaller than this.

Hence, one can theoretically expect τ/T, i.e., the relative intensity of the ghost PSF, to be somewhere between $\sim 1.2\,10^{-5}$ and $5.6\,10^{-5}$. The lower bound of this range is in a remarkable agreement with the peak-to-peak ratio observed experimentally, and the refresh time of the DMD appears to be at the origin of the ghost PSF.

One could potentially use a shutter synced with the DMD to mask the beam during the refresh. We have not attempted to set up this mechanism on the bench, and we may investigate this in the future, although the very short duration of the refresh could make it difficult. It is also not clear whether this ghost PSF would be critical for the observations.

5. CONCLUSIONS AND PERSPECTIVES

The CIDRE testbed, by combining phase and amplitude control, has made it possible to test out the capability of a DMD from TI to be used as an amplitude apodizer. The AO system that has been installed, using a 73×73 SH WFS, and a low-order 11×11 DM successfully corrects the wavefront down to 15 nm RMS (~ 10 nm for aberrations below 5cyc/pup). In addition, a NCPA calibration method that uses the science images was developed to increase the Strehl ratio of the PSF, improving it by 40%.

The DMD was used to apodize the wavefront corrected beam and create high-contrast regions around the star based on apodization patterns first computed for the high-contrast module of ELT-HARMONI. A demonstration was made that the fringes induced by a few missing segments of the M1 mirror could be efficiently corrected using the DMD, and that the average contrast that was obtained without missing segments could be recovered in spite of them. Contrasts down to 10^{-6} at $\sim 10\,\lambda/D$ of the star have been obtained, in agreement with the design.

Because of its control properties, the DMD induces a faint un-apodized PSF that is superimposed on the apodized PSF. The intensity of its peak has been measured to be $\sim 1.3\,10^{-5}$, relative to the peak intensity of an un-apodized PSF induced by a clear aperture displayed on the DMD, and it is not a limitation given the contrast level that the testbed was designed for.

Focal plane masks and Lyot stops will be added to the testbed in the coming months to test an adaptive APLC coronagraph. We also plan on using the testbed to create small dark holes next to the star, either by controlling the phase with the DM, or the amplitude with the DMD, or a combination of both, and a monomode fiber may be installed to try and optimize the commands sent to the DM and DMD so as to minimize the coupling of the electric field in the fiber core.

The main limitation of TI DMD remains its high chromaticity, due to the impossibility of keeping mirrors in a flat state with respect to the DMD wafer (each mirror has to be tilted positively or negatively, inducing a blazed grating pattern on the surface of the DMD).

We have identified two possible alternatives to the current device:

- a Phase Light Modulator (PLM [16]) recently developed by TI, with ~ 1000 actuators across. This is a prototype with a limited stroke capability ($\sim 250nm$ PTV), a limited dynamics (16 phase steps), and a high $> 5kHz$ control frequency. If these limitations are overcome in future PLMs, they could be used as adaptive phase apodizers, and maybe as second stage very high-order deformable mirrors, or as a tool to replicate AO residuals in the laboratory.

- micro-mirror arrays with ~ 300 actuators across have been developed at the Fraunhofer Institute [6]. Devices capable of piston or tip-tilt capabilities have been manufactured. The current stroke of the piston MMA is $0.5\mu m$, and should be increased up to $1\mu m$ and maybe more. As in the previous case, this device could be used as an adaptive phase apodizer or second stage DM. The number of actuators already makes it an interesting technology for an extreme AO system for the European ELT. The tip-tilt MMA is capable of continuous deflection, within a ± 3 deg range. Mirrors can thus be kept with a zero deflection angle, allowing them to reflect light without dispersing light, making this device a potential broadband binary amplitude controller. In both cases, the control frequency is $> 3.5kHz$ for pre-loaded patterns. The real time control frequency is currently limited to a much lower value (which would be fine for amplitude control), though a new electronics is being developed to perform real-time control at the same $3.5kHz$ frequency.

We intend to determine whether the specifications of these alternative devices satisfy the constraints of high-contrast imaging. The somewhat limited number of actuators across the pupil - a few hundreds - appears to be enough to lower the relative intensity of the diffracted light in the high-contrast region down to at least 10^{-8} using shaped pupils by themselves. Besides, these apodization patterns could be used together with other focal and pupil masks to further increase the contrast. Apodization patterns could also be computed to shape the PSF when trying to inject the light of off-axis companions in a monomode fiber.

Another specification that should be investigated is the refresh rate of these devices: the state of each actuator must be refreshed regularly to avoid actuators being stuck in a specific state, and this may happen at a high frequency. It is unclear at the moment if this could be an issue when controlling the phase or the amplitude. In the case of amplitude modulation, it appears possible to keep co-planar micro-mirrors in their state without any issue, and to keep the other micro-mirrors moving by inducing a continuous rotation of the reflected beam around the normal to the array for each micro-mirror.

Note that such devices would also be very useful laboratory tools, both for R&D projects, and for MAIT activities.

ACKNOWLEDGMENTS

This project is funded by the European Research Council (ERC) under the European Union's Horizon 2020 research and innovation programme (grant agreement n°866001 - EXACT).

References

[1] Petra Aswendt and Roland Hoefling. "Industrial DLP Projection Technology". In: *Proceedings of the International Display Workshops* (Nov. 2019), p. 1313. DOI: 10.36463/IDW.2019.PRJ4-4.

[2] J. -L. Beuzit et al. "SPHERE: the exoplanet imager for the Very Large Telescope". In: 631, A155 (Nov. 2019), A155. DOI: 10.1051/0004-6361/201935251. arXiv: 1902.04080 [astro-ph.IM].

[3] A. Carlotti, R. Vanderbei, and N. J. Kasdin. "Optimal pupil apodizations of arbitrary apertures for high-contrast imaging". In: *Optics Express* 19.27 (Dec. 2011), p. 26796. DOI: 10.1364/OE.19.026796.

[4] Alexis Carlotti et al. "Experimental test of a micro-mirror array as an adaptive apodizer for high-contrast imaging". In: *Advances in Optical and Mechanical Technologies for Telescopes and Instrumentation III*. Ed. by Ramón Navarro and Roland Geyl. Vol. 10706. Society of Photo-Optical Instrumentation Engineers (SPIE) Conference Series. July 2018, 107062M, p. 107062M. DOI: 10.1117/12.2311974.

[5] Alexis Carlotti et al. "HARMONI at ELT: system analysis and performance estimation of the high-contrast module". In: *Adaptive Optics Systems VIII*. Ed. by Laura Schreiber, Dirk Schmidt, and Elise Vernet. Vol. 12185. Society of Photo-Optical Instrumentation Engineers (SPIE) Conference Series. Aug. 2022, 121855L, p. 121855L. DOI: 10.1117/12.2628927.

[6] A. Gehner et al. "Novel CMOS-integrated 512x320 tip-tilt micro mirror array and related technology platform". In: *MOEMS and Miniaturized Systems XIX*. Ed. by Wibool Piyawattanametha, Yong-Hwa Park, and Hans Zappe. Vol. 11293. Society of Photo-Optical Instrumentation Engineers (SPIE) Conference Series. Feb. 2020, 1129302, p. 1129302. DOI: 10.1117/12.2543052.

[7] Julien H. Girard et al. "JWST/NIRCam coronagraphy: commissioning and first on-sky results". In: *Space Telescopes and Instrumentation 2022: Optical, Infrared, and Millimeter Wave*. Ed. by Laura E. Coyle, Shuji Matsuura, and Marshall D. Perrin. Vol. 12180. Society of Photo-Optical Instrumentation Engineers (SPIE) Conference Series. Aug. 2022, 121803Q, 121803Q. DOI: 10.1117/12.2629636. arXiv: 2208.00998 [astro-ph.IM].

[8] O. Guyon. "Phase-induced amplitude apodization of telescope pupils for extrasolar terrestrial planet imaging". In: 404 (June 2003), pp. 379–387. DOI: 10.1051/0004-6361:20030457. arXiv: astro-ph/0301190 [astro-ph].

[9] Olivier Guyon et al. "High contrast and high angular imaging at Subaru Telescope". In: *Adaptive Optics Systems VIII*. Ed. by Laura Schreiber, Dirk Schmidt, and Elise Vernet. Vol. 12185. Society of Photo-Optical Instrumentation Engineers (SPIE) Conference Series. Aug. 2022, 121856J, 121856J. DOI: 10.1117/12.2630534. arXiv: 2208.01809 [astro-ph.IM].

[10] Lucie Leboulleux et al. "Coronagraphy for DiRect Imaging of Exoplanets (CIDRE) testbed 1: concept, optical set up, and experimental results of adaptive amplitude apodization". In: *Society of Photo-Optical Instrumentation Engineers (SPIE) Conference Series*. Vol. 12188. Society of Photo-Optical Instrumentation Engineers (SPIE) Conference Series. Aug. 2022, 121884J, 121884J. DOI: 10.1117/12.2629318. arXiv: 2209.05862 [astro-ph.IM].

[11] Bruce A. Macintosh et al. "The Gemini planet imager: first light and commissioning". In: *Adaptive Optics Systems IV*. Ed. by Enrico Marchetti, Laird M. Close, and Jean-Pierre Vran. Vol. 9148. Society of Photo-Optical Instrumentation Engineers (SPIE) Conference Series. Aug. 2014, 91480J, 91480J. DOI: 10.1117/12.2056709.

[12] Jared R. Males et al. "MagAO-X: current status and plans for Phase II". In: *Adaptive Optics Systems VIII*. Ed. by Laura Schreiber, Dirk Schmidt, and Elise Vernet. Vol. 12185. Society of Photo-Optical Instrumentation Engineers (SPIE) Conference Series. Aug. 2022, 1218509, p. 1218509. DOI: 10.1117/12.2630584. arXiv: 2208.07299 [astro-ph.IM].

[13] P. Martinez et al. "Halftoning for high-contrast imaging". In: *European Physical Journal Web of Conferences*. Vol. 16. European Physical Journal Web of Conferences. July 2011, 03003, p. 03003. DOI: 10.1051/epjconf/20111603003.

[14] J. Mazoyer et al. "Active Correction of Aperture Discontinuities-Optimized Stroke Minimization. I. A New Adaptive Interaction Matrix Algorithm". In: 155.1, 7 (Jan. 2018), p. 7. DOI: 10.3847/1538-3881/aa91cf. arXiv: 1709.02406 [astro-ph.IM].

[15] B. Mennesson et al. "The Roman Space Telescope coronagraph technology demonstration: current status and relevance to future missions". In: *Space Telescopes and Instrumentation 2022: Optical, Infrared, and Millimeter Wave*. Ed. by Laura E. Coyle, Shuji Matsuura, and Marshall D. Perrin. Vol. 12180. Society of Photo-Optical Instrumentation Engineers (SPIE) Conference Series. Aug. 2022, 121801W, 121801W. DOI: 10.1117/12.2629176.

[16] Bing Ouyang et al. "Evaluating Texas instruments Phase Light Modulator (PLM)". In: *Ocean Sensing and Monitoring XIV*. Ed. by Weilin "Will" Hou and Linda J. Mullen. Vol. 12118. Society of Photo-Optical Instrumentation Engineers (SPIE) Conference Series. May 2022, 121180I, p. 121180I. DOI: 10.1117/12.2623938.

[17] Laurent Pueyo and Colin Norman. "High-contrast Imaging with an Arbitrary Aperture: Active Compensation of Aperture Discontinuities". In: 769.2, 102 (June 2013), p. 102. DOI: 10.1088/0004-637X/769/2/102. arXiv: 1211.6112 [astro-ph.IM].

[18] Laurent Pueyo et al. "Optimal dark hole generation via two deformable mirrors with stroke minimization". In: 48.32 (Nov. 2009), p. 6296. DOI: 10.1364/AO.48.006296.

[19] Sophia R. Vaughan et al. "Chasing rainbows and ocean glints: Inner working angle constraints for the Habitable Worlds Observatory". In: 524.4 (Oct. 2023), pp. 5477–5485. DOI: 10.1093/mnras/stad2127. arXiv: 2307.15137 [astro-ph.EP].

[20] Gillian S. Wright et al. “The Mid-infrared Instrument for JWST and Its In-flight Performance”. In: 135.1046, 048003 (Apr. 2023), p. 048003. DOI: 10.1088/1538-3873/acbe66.

[21] Frederic Zamkotsian et al. “Batman flies: a compact spectro-imager for space observation”. In: *Society of Photo-Optical Instrumentation Engineers (SPIE) Conference Series*. Vol. 10563. Society of Photo-Optical Instrumentation Engineers (SPIE) Conference Series. Nov. 2017, 105634N, 105634N. DOI: 10.1117/12.2304262.